

Non-galvanic calibration and operation of a quantum dot thermometer

J. M. A. Chawner,* S. Holt, E. A. Laird, Yu. A. Pashkin, and J. R. Prance
Department of Physics, Lancaster University, Lancaster, LA1 4YB, United Kingdom

S. Barraud
CEA/LETI-MINATEC, CEA-Grenoble, 38000 Grenoble, France

M. F. Gonzalez-Zalba
Hitachi Cambridge Laboratory, J. J. Thomson Ave., Cambridge, CB3 0HE, United Kingdom[†]
(Dated: January 29, 2021)

A cryogenic quantum dot thermometer is calibrated and operated using only a single non-galvanic gate connection. The thermometer is probed with radio-frequency reflectometry and calibrated by fitting a physical model to the phase of the reflected radio-frequency signal taken at temperatures across a small range. Thermometry of the source and drain reservoirs of the dot is then performed by fitting the calibrated physical model to new phase data. The thermometer can operate at the transition between thermally broadened and lifetime broadened regimes, and outside the temperatures used in calibration. Electron thermometry was performed at temperatures between 3.0K and 1.0K, in both a 1K cryostat and a dilution refrigerator. In principle, the experimental setup enables fast electron temperature readout with a sensitivity of $4.0 \pm 0.3 \text{ mK}/\sqrt{\text{Hz}}$, at kelvin temperatures. The non-galvanic calibration process gives a readout of physical parameters, such as the quantum dot lever arm. The demodulator used for reflectometry readout is readily available and very affordable.

I. INTRODUCTION

Electron temperature is a fundamental parameter that can limit the performance of low-temperature experiments and applications. Electron thermometry is an essential tool in understanding the behaviour of low-temperature circuitry [1], for example the processors used in quantum computers or devices used to study exotic electronic phases and materials. Accurate and fast electron temperature readout is also a valuable tool for thermodynamic experiments. Increasingly sensitive quantum circuits require delicate and non-invasive electronic thermometry. Quantum dot (QD) and single-electron transistor (SET) conduction thermometry are well established as a powerful approach to monitor electron temperatures [1–11]. However, these thermometers require the measurement of current through the QD, which can complicate or interfere with other electronic measurements in the experiment. Furthermore, the extra galvanic connections for dot thermometry can be a source of additional noise and parasitic heating. Local charge sensing can be used to probe the occupation of a QD without having to pass a direct current through it [5, 12–15]. This approach still requires galvanic connections to read the charge sensor. Similarly, radio frequency (RF) reflectometry techniques have recently allowed QD thermometry to be performed without measuring current through the QD, which is effective outside the lifetime broadened regime [16, 17]. However, for both charge sensing and reflectometry, connections to the source and drain of the dot are still needed to measure the dot lever arm for calibration.

Here we demonstrate how a completely non-galvanic QD thermometer can be calibrated and used with a single capac-

itive gate connection, including a calibration of the lever arm with no DC source-drain bias. The QD thermometer has the flexibility to be used on any conducting reservoir and operates in an intermediate regime where the maximum temperature is much lower than the QD charging energy $k_B T \ll E_c$ and the minimum temperature is similar to the tunnel coupling $k_B T \sim \hbar\Gamma$.

II. EXPERIMENTAL DETAILS

The QD device used in our experiment is a silicon-on-insulator trigate accumulation-mode field-effect transistor (FET) with a channel length, width and height of 80nm, 30nm and 10nm respectively, shown in Fig 1a and b. For more details about the device, see reference [18]. At cryogenic temperatures, when a positive sub-threshold DC voltage V_{tg} is applied to the top gate, a localisation potential appears in the Si channel underneath the gate. This allows bound electron states to accumulate, and creates a single QD. Corner dots [19, 20] do not appear in the structure due to the narrow width of the channel. The FET top gate also acts as a plunger gate for the QD via capacitance C_{tg} , allowing tuning of the next available energy level in the QD, which is labelled E_{QD} , by adjusting V_{tg} . The source and drain electrodes are both grounded and act as a single reservoir of electrons with a Fermi level μ (Fig 1c). Throughout the experiment, the back gate was grounded.

The QD energy level E_{QD} is broadened by tunnel coupling to the reservoir [21, 22]. This is described with a broadened density of states in the form of a normalised Lorentzian, given by:

$$n(E_{\text{QD}}, E) = \frac{1}{\pi} \frac{\hbar\Gamma}{(E_{\text{QD}} - E)^2 + (\hbar\Gamma)^2}, \quad (1)$$

where \hbar is the reduced Planck's constant [21]. The tun-

* j.chawner@lancaster.ac.uk

[†] Present address: Quantum Motion Technologies, Windsor House, Corn-wall Road, Harrogate, England, HG1 2PW

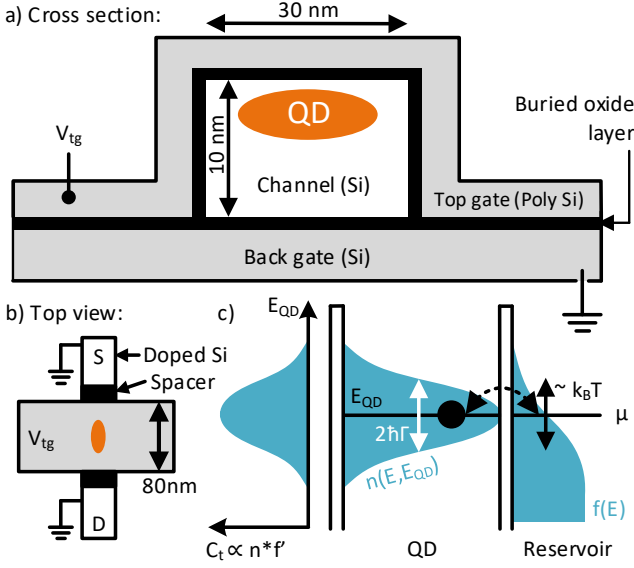


FIG. 1. Details of the silicon field-effect transistor QD. **a)** Cross-section schematic of the device. The transistor consists of an undoped 1-D Si channel, 10nm high by 30nm wide, with n-doped Si source-drain connections. A polycrystalline silicon top gate, 80nm wide, bridges over the channel, separated by a layer of SiO₂. A grounded Si back gate is beneath the channel, separated from the channel by 145nm thick buried SiO₂. **b)** Top view of device. The source (S) and drain (D) channel connection points are n-doped and behave as a single grounded reservoir during thermometry operation. Two spacers are used to prevent doping of the Si channel under the top gate. **c)** Energy diagram of the system. The reservoir has an occupation of electron states given by the Fermi-Dirac distribution f . The QD energy level E_{QD} is broadened from tunnel coupling to the reservoir, with a density of states n described by Eq. (1). The tunnelling capacitance C_t as a function of E_{QD} has a shape proportional to $f' * n$.

nel rate Γ between the QD and the reservoir is given by $\Gamma = \Gamma_s \Gamma_d / (\Gamma_s + \Gamma_d)$, where $\Gamma_s(d)$ is the tunnel rate through source(drain) barrier. The probability P_{QD} of an excess electron occupying the QD is given by the integral of the product of $n(E_{\text{QD}}, E)$ and the Fermi-Dirac distribution of electrons in the reservoir $f(E)$ [21]:

$$P_{\text{QD}}(E_{\text{QD}}) = \int_{-\infty}^{\infty} f(E) n(E_{\text{QD}}, E) dE. \quad (2)$$

This is the convolution of the two functions, so P_{QD} becomes:

$$P_{\text{QD}}(E_{\text{QD}}) = (f * n). \quad (3)$$

Due to the spin degeneracy of the extra electron in the QD, $P_{\text{QD}} = 1/2$ occurs when $E_{\text{QD}} = \mu \pm k_B T \ln 2$ [17, 23]. The QD has both a constant geometric capacitance and a variable ‘tunneling’ capacitance C_t , given by [17, 24–28]:

$$C_t(V_{\text{tg}}) = e\alpha \frac{\partial P_{\text{QD}}}{\partial V_{\text{tg}}}, \quad (4)$$

where $\alpha = C_{\text{tg}}/C_{\Sigma}$ is the top gate lever arm, C_{Σ} is the total QD capacitance, $\partial V_{\text{tg}} = -\partial E_{\text{QD}}/e\alpha$, and e is the elementary

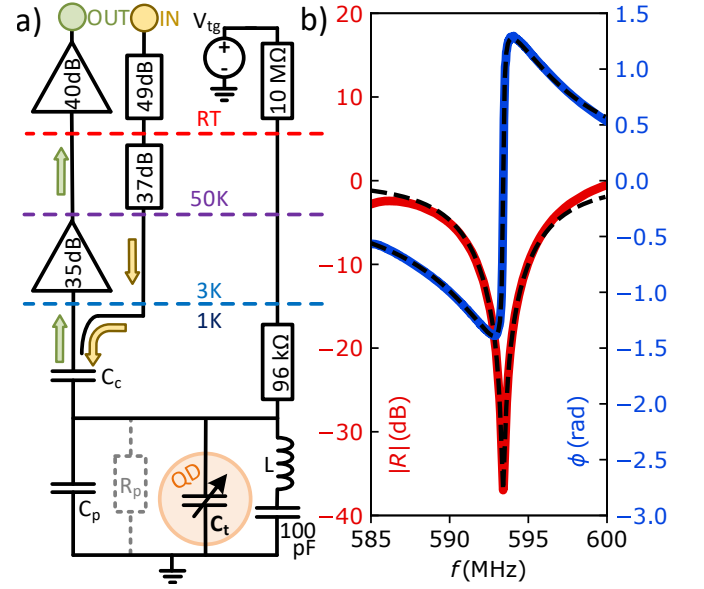


FIG. 2. Details of RF circuitry. **a)** Schematic of the circuit layout. The resonant circuit is comprised of the NbTiN-on-quartz spiral inductor L , the parasitic capacitance C_p , coupling capacitance C_c and the variable QD tunnelling capacitance C_t , which is the physical parameter monitored for thermometry. C_p includes the geometric gate capacitance C_{tg} for modelling purposes. R_p is a modelled parasitic loss resistance to ground which impacts the resonant circuit Q-factor. The inductor line has a 100pF capacitor to provide a DC break between the top gate and ground. The 96kΩ resistor limits top gate RF signal loss to the DC line. V_{tg} is the controllable DC top gate voltage. IN and OUT represent the RF reflectometry input and output signal, respectively. **b)** The loaded measurement circuit resonance when coupled to the top gate, with the reflected signal magnitude $|R|$ and phase ϕ shown in red and blue, respectively. The black dashed lines show the fitted circuit model, which measures a Q-factor of 63. Thermometry is performed on resonance at $f_0 = 593$ MHz, where phase is most responsive.

charge. Inserting Eq. (3) into this definition gives us the tunnelling capacitance of the QD-reservoir system:

$$C_t(V_{\text{tg}}) = e\alpha (f * n)' = e\alpha (f' * n). \quad (5)$$

The derivative of f with respect to V_{tg} , denoted f' , is

$$f'(V_{\text{tg}}) = \frac{1}{4k_B T_e} \cosh^{-2} \left(\frac{-\alpha e (V_{\text{tg}} - V_0)}{2k_B T_e} \right), \quad (6)$$

where T_e is the electron temperature of the reservoirs, V_0 is the value of V_{tg} when $P_{\text{QD}} = 1/2$, and k_B is the Boltzmann constant. The T_e dependence of C_t via Eq. (6) is the basis for the non-galvanic QD thermometer.

The capacitance C_t was measured by RF reflectometry using the setup shown in Fig 2a. A resonant circuit was connected to the QD top gate and consisted of a NbTiN-on-quartz spiral inductor $L = 96$ nH, and a coupling capacitor $C_c = 0.18$ pF. The inductor is placed parallel to the measured capacitance to help improve the loaded Q-factor, which helps achieve a larger signal for a given change in capacitance [29]. Modelling the circuit using the measured RF reflection $|R|$ and

phase ϕ (shown in Fig 2b) gives a resonance frequency of $f_0 = 593.4$ MHz with a Q-factor of 63, a parasitic capacitance of $C_p = 0.57$ pF and a parasitic resistance of $R_p = 43.2$ k Ω . A modelled circuit loss to ground is represented by resistance R_p , which affects the resonance Q-factor [29]. The parasitic capacitance C_p includes the geometric gate capacitance C_{tg} . The demodulation of $|R|$ and ϕ was performed with an ‘ADL5387’ active quadrature demodulator chip. To allow a DC bias V_{tg} to be applied to the top gate, a 100 pF capacitor was placed after the inductor to avoid DC-shorting the device and to create a good RF ground at the frequency of operation. A 96 k Ω resistor was used to prevent RF signals from escaping via the DC bias line. The resonant frequency depends on total top gate capacitance via $f_0 = 1/2\pi\sqrt{L(C_c + C_p + C_t)}$. At the circuit resonant frequency, $\phi \propto C_t$, when $C_t \ll C_p + C_c$ [17, 28, 30–32]. This gives a change in reflected signal phase that depends on T_e according to:

$$\phi - \phi_0 = Ae\alpha (f' * n), \quad (7)$$

where A is a fitting constant, which tells us the phase change due to a small change in capacitance, and ϕ_0 is the circuit phase offset at the resonant frequency when $C_t \approx 0$. If the constants A , α and Γ are known, measuring $\phi - \phi_0$ as a function of $V_{tg} - V_0$ and fitting the model described by Eq. (7) gives a readout of electron temperature T_e . A demonstration of this technique is shown in Fig 3.

III. RESULTS

The QD thermometer was measured in two fridge systems: a cryogen-free 1 K cryostat¹ and a cryogen-free dilution refrigerator², where it was calibrated and operated. In both systems, the fridge temperature was monitored by a ruthenium oxide resistance fridge thermometer³ mounted alongside the QD thermometer during data collection. The reading of the ruthenium oxide fridge thermometer is denoted as T_f .

In the 1 K cryostat, calibration was done by reading the reflected signal phase across a number of sweeps of V_{tg} at a set of fridge temperatures $T_f = 2.0, 2.5, 3.0$ K. A single least-squares fit using Eq. (7) was performed on the collective phase traces for this set of temperatures (Fig 3). It was assumed that the electron temperature is well thermalised with the fridge temperature at 2 K and above, and so during the calibration the condition $T_e = T_f$ was applied to Eq. (7). For each phase trace, ϕ_0 and V_0 were individually fitted. The calibration fit produced an estimate for the values $\alpha = 0.74 \pm 0.02$, $\Gamma = 270 \pm 20$ ns⁻¹ and $A = 5.13 \pm 0.06$ rad pF⁻¹. This implies $\Gamma \gg 2\pi f_0$, therefore dissipative components were neglected and the cyclic tunnelling was considered adiabatic. With these three constants defined, the thermometer was calibrated and ready for operation.

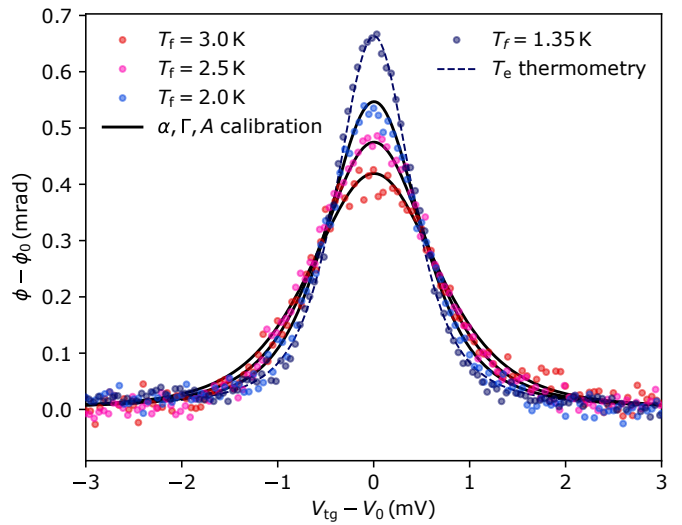


FIG. 3. QD thermometer calibration in 1K cryostat, showing three experimental phase traces taken at fridge temperatures $T_f = 2.0, 2.5, 3.0$ K. Each trace shows the change in reflected signal phase $\phi - \phi_0$ against top gate voltage $V_{tg} - V_0$ around the Coulomb peak of the QD. The solid black lines show the least-square fit of Eq. (7) onto the data, assuming the electron temperature T_e equals the fridge thermometer readout T_f . This calibration procedure estimates $\alpha = 0.74 \pm 0.02$, $\Gamma = 270 \pm 20$ ns⁻¹ and $A = 5.13 \pm 0.06$ rad pF⁻¹. These three constants are then included within Eq. (7), allowing electron thermometry to be performed, shown here with a T_e fit to data taken at $T_f = 1.35$ K, yielding an electron temperature $T_e = 1.4 \pm 0.1$ K

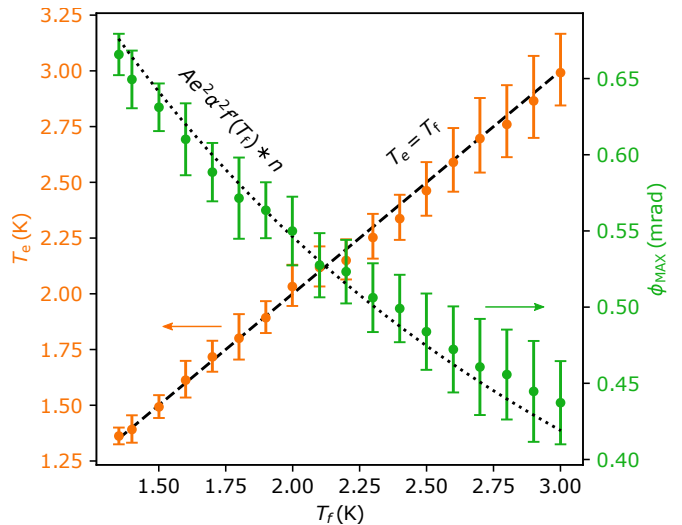


FIG. 4. Electron temperature T_e (orange) and max phase ϕ_{MAX} (green) readout from QD thermometer in 1K cryostat. Thermometry readout was generated by fitting T_e , via calibrated Eq. (7), to the phase curve observed by sweeping the V_{tg} over the QD Coulomb peak. The peak phase ϕ_{MAX} was measured at $V_{tg} = V_0$, with no fitting process required. The fridge temperature T_f was read from a ruthenium oxide fridge thermometer thermally linked to the QD device. The dashed line highlights where $T_e = T_f$. The dotted line represents the model prediction from calibrated Eq. (7), assuming $T_e = T_f$.

¹ Oxford Instruments ‘Io’

² BlueFors ‘LD250’

³ Model ref ‘ROTH-GEN’ in the 1K cryostat and ‘RuO2.RX-102B’ in the dilution refrigerator

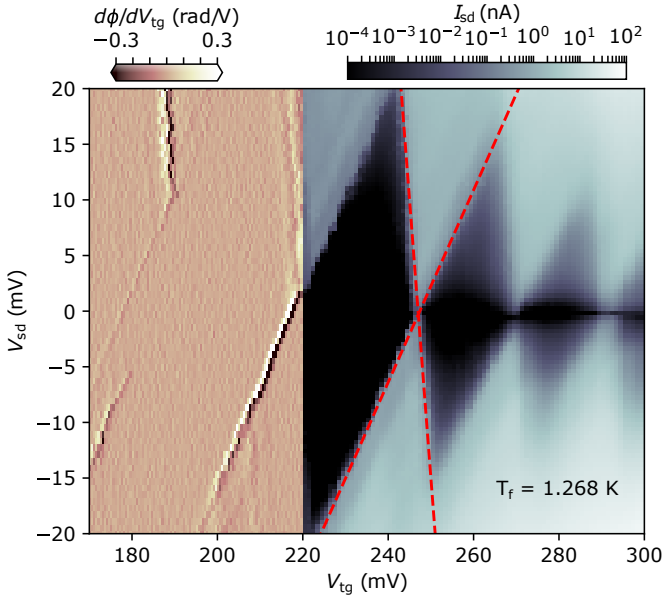


FIG. 5. Charge stability diagram measured by reflectometry technique and DC transport in 1 K cryostat. To the left of $V_{tg} = 220$ mV, the derivative of reflected signal phase with respect to the top gate voltage $d\phi/dV_{tg}$ is plotted, demonstrating the non-galvanic reflectometry technique. For this measurement, the source and drain connections were grounded. To the right of $V_{tg} = 220$ mV, the QD source-drain current $|I_{sd}|$ is plotted in log scale. The fridge temperature was $T_f = 1.268 \pm 0.001$ K. Red lines highlight the source-drain gradients that match the calibration fit lever arm prediction, $\alpha = 0.74 \pm 0.02$, via Eq. (8), crossing at the QD Coulomb peak where the thermometry took place. Here the on-resonance current has an order of magnitude $I_{sd} \approx 1 - 10$ nA, which is similar to the single-electron current defined by the calibration fit tunnel rate $e\Gamma \sim 6.9 \pm 0.5$ nA.

To use the QD thermometer, $\phi - \phi_0$ was measured as a function of $V_{tg} - V_0$ and fitted with the calibrated Eq. (7) to give a readout of electron temperature T_e . A series of thermometry readings were taken at varying fridge temperatures between 3.0 K and 1.3 K. Fridge temperature T_f was monitored for each QD thermometer reading of T_e (Fig 4). The QD thermometer agreed with the fridge thermometer across the range of temperatures, even at temperatures below the calibration range. It is worth noting that this works in the intermediate regime where $k_B T \sim \hbar\Gamma$ because the tunnel broadening is taken into account within the physical model. For quicker electron temperature readout, the QD can be tuned to where $V_{tg} = V_0$ so that $\phi - \phi_0 = \phi_{MAX}$, which was directly converted to a electron temperature via Eq. (7), using the previously calibrated values of α , Γ and A . This approach worked effectively, even at fridge temperatures below the calibration data.

Finally, to provide an independent confirmation of the calibration process, the QD source and drain connections were ungrounded to apply a source-drain voltage V_{sd} across the QD and measure a charge stability diagram of the device. Using the relationship

$$\alpha = \frac{1}{m_d - m_s}, \quad (8)$$

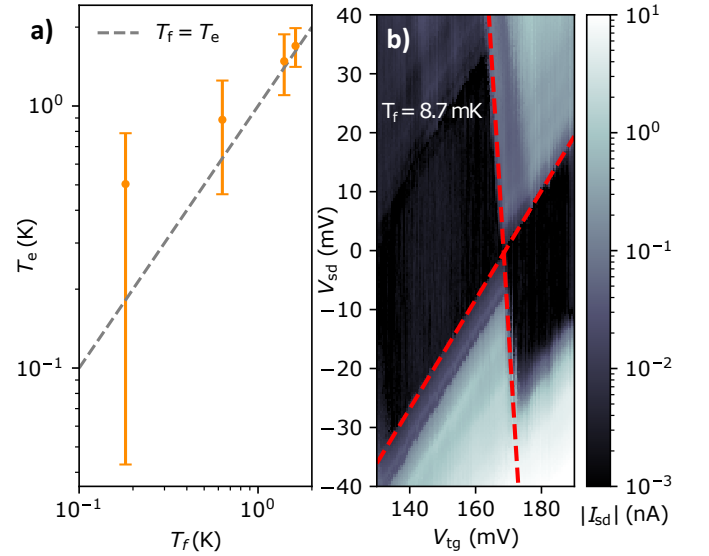


FIG. 6. QD Thermometry and stability diagram from dilution refrigerator measurements. **a)** Re-calibrated QD thermometer readout of electron temperature T_e compared with fridge thermometer readout T_f , measured near the device within the dilution refrigerator. The QD and fridge thermometers start to disagree below 1 K, but still agree within one standard deviation of confidence (For details on how the error is determined, see section II in the Supplemental Material [33]). **b)** Source-drain current stability diagram of QD mounted in dilution refrigerator. The temperature of the fridge was held at $T_f = 8.70 \pm 0.05$ mK. Red lines highlight the source-drain gradients that match the calibration fit lever arm prediction, $\alpha = 0.84 \pm 0.03$, via Eq. (8), crossing at the QD Coulomb peak where the thermometry took place.

where $m_d = \Delta V_{tg}^d / \Delta V_{sd}^d$ is the gradient along the the ‘drain resonance’ side of a Coulomb diamond and $m_s = \Delta V_{tg}^s / \Delta V_{sd}^s$ is the ‘source resonance’ side, we can see the lever arm $\alpha = 0.74 \pm 0.02$ matches well with the Coulomb diamond geometry in Fig 5. This demonstrates that the lever arm of a QD can be obtained using one non-galvanic gate connection and measurements spanning a range of fridge temperatures. The order of magnitude of source-drain current $|I_{sd}|$ from the unblocked QD was found to be in the order of ~ 10 nA. This agrees with the calibration fit of the total tunnel rate constant 270 ± 20 ns $^{-1}$, which equates to a source-drain current of $e\Gamma = 6.9 \pm 0.5$ nA for a single electron transport channel.

To study operation at lower temperatures, the QD thermometer was mounted into a dilution refrigerator. The calibration fit was performed as described above, with phase data taken at 1300 mK and 1600 mK. Within this system, the three calibration constants were found to be $\alpha = 0.84 \pm 0.03$, $\Gamma = 510 \pm 10$ ns $^{-1}$ and $A = 0.75 \pm 0.07$ rad pF $^{-1}$. The change in A is attributed to the differences between the two fridge systems affecting the RF electronics, such as parasitic capacitance C_p changing due to a different metallic geometry near to the QD chip. Both α and Γ are sensitive to the shape and position of the QD in the Si channel, which are likely to be different after a thermal cycle of the device.

The electron temperature readout T_e from the QD ther-

meter in the dilution refrigerator agreed with the fridge temperature readout T_f above 1 K, despite the fact that $k_B T_f < \hbar\Gamma$ (Fig 6a). Below 1 K there was deviation of T_e away from T_f , although the point $T_e = T_f$ remains within one standard deviation of experimental uncertainty (For details on how the error is determined, see section II in the Supplemental Material [33]). The deviation of T_e readout and its increase in uncertainty occurs because the QD energy level is strongly tunnel-broadened and the response of the phase trace to temperature becomes weaker (For details on the influence of tunnel broadening, see section III and FIG. 4 in the Supplemental Material [33]). With a reduced Γ the QD thermometer would work at lower temperatures. This can be achieved by adjusting the device design geometry. Checking the charge stability diagram, the predicted lever arm $\alpha = 0.84 \pm 0.03$ matches the Coulomb diamond geometry well (Fig 6b). The dilution refrigerator experiment has an average white noise phase sensitivity of $1.1 \pm 0.1 \mu\text{rad}/\sqrt{\text{Hz}}$, in this case dominated by the measurement chain. With this equipment and the ϕ_{MAX} measurements demonstrated in Fig 4, the QD thermometer setup could achieve a potential sensitivity of $11 \pm 1 \text{mK}/\sqrt{\text{Hz}}$ at 3.0 K, and $4.0 \pm 0.3 \text{mK}/\sqrt{\text{Hz}}$ at 1.3 K (For details on the thermometer sensitivity, see section I in the Supplemental Material [33]).

IV. CONCLUSIONS

We have described the successful calibration and operation of a QD thermometer readout via a single capacitive connection in two separate cryostats, which introduces a new level of simplicity and versatility for measuring electron temperature. The calibration uses limited data to generate a physical model of the QD-reservoir system, which correctly estimates

physical parameters such as the QD lever arm. Electron thermometry was successfully performed with the calibrated QD thermometer in a 1.0 K to 3.0 K range. The QD thermometer was also used for faster readout by monitoring the phase when the QD has an occupation probability of 1/2. In this mode of operation, the noise floor of the measurement should allow for a sensitivity of $4.0 \pm 0.3 \text{mK}/\sqrt{\text{Hz}}$ and $11 \pm 1 \text{mK}/\sqrt{\text{Hz}}$, at 1.3 K and 3.0 K respectively. This process worked with the same QD chip in both cryostats. The QD thermometer can operate even in the case where $k_B T_e < \hbar\Gamma$, however with the system and techniques used here, the thermometry uncertainty starts to increase below 1 K due to strong tunnel coupling overriding the temperature dependence. Careful analysis of the thermometry uncertainty reveals the coldest limit of the QD thermometer, when the electron temperature readout confidence boundary increases beyond a usable size. A redesign of the QD device to reduce the tunnel rate would be needed to decrease the uncertainty at lower temperatures. The ability to fully calibrate and operate a non-galvanic electron thermometer with a single RF line simplifies the application of the device substantially. This device provides a versatile, sensitive and effective tool for monitoring electron temperature in nanoelectronic devices at cryogenic temperatures.

ACKNOWLEDGMENTS

We thank Xiao Collins, Kunal Lulla Ramrakhiani, Michael Thompson and Alex Jones for their assistance.

This work was funded and supported by the European Microkelvin Platform (the European Union's Horizon 2020 research and innovation programme, Grant Agreement No. 824109), the UK EPSRC (EP/N019199/1), the ERC (818751) and Hitachi Europe Ltd.

The data that support the findings of this study are available at <https://doi.org/10.17635/lancaster/researchdata/403>, including descriptions of the data sets.

-
- [1] F. Giazotto, T. T. Heikkilä, A. Luukanen, A. M. Savin, and J. P. Pekola, *Opportunities for mesoscopics in thermometry and refrigeration: Physics and applications*, Rev. Mod. Phys. **78**, 217 (2006).
 - [2] C. Beenakker, *Theory of coulomb-blockade oscillations in the conductance of a quantum dot*, Phys. Rev. B **44**, 1646 (1991).
 - [3] J. Pekola, K. Hirvi, J. Kauppinen, and M. Paalanen, *Thermometry by arrays of tunnel junctions*, Phys. Rev. Lett. **73**, 2903 (1994).
 - [4] L. Spietz, K. Lehnert, I. Siddiqi, and R. Schoelkopf, *Primary electronic thermometry using the shot noise of a tunnel junction*, Science **300**, 1929 (2003).
 - [5] D. Maradan, L. Casparis, T.-M. Liu, D. Biesinger, C. Scheller, D. Zumbühl, J. Zimmerman, and A. Gossard, *Gaas quantum dot thermometry using direct transport and charge sensing*, J. Low Temp. Phys. **175**, 784 (2014).
 - [6] J. V. Koski, A. Kutvonen, I. M. Khaymovich, T. Ala-Nissila, and J. P. Pekola, *On-chip maxwell's demon as an information-powered refrigerator*, Phys. Rev. Lett. **115**, 260602 (2015).
 - [7] D. I. Bradley, R. E. George, D. Gunnarsson, R. P. Haley, H. Heikkinen, Y. A. Pashkin, J. Penttilä, J. R. Prance, M. Prunnila, L. Roschier, *et al.*, *Nanoelectronic primary thermometry below 4 mk*, Nat. Commun. **7**, 1 (2016).
 - [8] O. Hahtela, E. Mykkänen, A. Kemppinen, M. Meschke, M. Prunnila, D. Gunnarsson, L. Roschier, J. Penttilä, and J. Pekola, *Traceable coulomb blockade thermometry*, Metrologia **54**, 69 (2016).
 - [9] Z. Iftikhar, A. Anthore, S. Jezouin, F. Parmentier, Y. Jin, A. Cavanaugh, A. Ouerghi, U. Gennser, and F. Pierre, *Primary thermometry triad at 6 mk in mesoscopic circuits*, Nat. Commun. **7**, 1 (2016).
 - [10] G. Nicolí, P. Märki, B. A. Bräm, M. P. Rössli, S. Hennel, A. Hofmann, C. Reichl, W. Wegscheider, T. Ihn, and K. Ensslin, *Quantum dot thermometry at ultra-low temperature in a dilution refrigerator with a 4he immersion cell*, Rev. Sci. Instrum. **90**, 113901 (2019).
 - [11] A. Jones, C. Scheller, J. Prance, Y. Kalyoncu, D. Zumbühl, and R. Haley, *Progress in cooling nanoelectronic devices to ultra-low temperatures*, J. Low Temp. Phys. (2020).
 - [12] L. DiCarlo, H. Lynch, A. Johnson, L. Childress, K. Crockett, C. Marcus, M. Hanson, and A. Gossard, *Differential charge sensing and charge delocalization in a tunable double quantum*

- dot*, Phys. Rev. Lett. **92**, 226801 (2004).
- [13] P. Torresani, M. Martínez-Pérez, S. Gasparinetti, J. Renard, G. Biasiol, L. Sorba, F. Giazotto, and S. De Franceschi, *Non-galvanic primary thermometry of a two-dimensional electron gas*, Phys. Rev. B **88**, 245304 (2013).
- [14] A. Mavalankar, S. Chorley, J. Griffiths, G. Jones, I. Farrer, D. Ritchie, and C. Smith, *A non-invasive electron thermometer based on charge sensing of a quantum dot*, Appl. Phys. Lett. **103**, 133116 (2013).
- [15] J. Prance, C. Smith, J. Griffiths, S. Chorley, D. Anderson, G. Jones, I. Farrer, and D. Ritchie, *Electronic refrigeration of a two-dimensional electron gas*, Phys. Rev. Lett. **102**, 146602 (2009).
- [16] S. Gasparinetti, K. Viisanen, O.-P. Saira, T. Faivre, M. Arzeo, M. Meschke, and J. Pekola, *Fast electron thermometry for ultrasensitive calorimetric detection*, Phys. Rev. Appl. **3**, 014007 (2015).
- [17] I. Ahmed, A. Chatterjee, S. Barraud, J. J. Morton, J. A. Haigh, and M. F. Gonzalez-Zalba, *Primary thermometry of a single reservoir using cyclic electron tunneling to a quantum dot*, Commun. Phys. **1**, 1 (2018).
- [18] A. Betz, S. Barraud, Q. Wilmart, B. Placais, X. Jehl, M. Sanquer, and M. Gonzalez-Zalba, *High-frequency characterization of thermionic charge transport in silicon-on-insulator nanowire transistors*, Appl. Phys. Lett. **104**, 043106 (2014).
- [19] B. Voisin, V.-H. Nguyen, J. Renard, X. Jehl, S. Barraud, F. Triozon, M. Vinet, I. Duchemin, Y.-M. Niquet, S. De Franceschi, *et al.*, *Few-electron edge-state quantum dots in a silicon nanowire field-effect transistor*, Nano letters **14**, 2094 (2014).
- [20] D. J. Ibberson, L. Bourdet, J. C. Abadillo-Uriel, I. Ahmed, S. Barraud, M. J. Calderón, Y.-M. Niquet, and M. F. Gonzalez-Zalba, *Electric-field tuning of the valley splitting in silicon corner dots*, Appl. Phys. Lett. **113**, 053104 (2018).
- [21] L. P. Kouwenhoven, C. M. Marcus, P. L. McEuen, S. Tarucha, R. M. Westervelt, and N. S. Wingreen, in *Mesoscopic electron transport* (Springer, 1997) pp. 105–214.
- [22] T. Ihn, *Semiconductor Nanostructures: Quantum States and Electronic Transport* (OUP Oxford, 2010).
- [23] N. Hartman, C. Olsen, S. Lüscher, M. Samani, S. Fallahi, G. C. Gardner, M. Manfra, and J. Folk, *Direct entropy measurement in a mesoscopic quantum system*, Nat. Phys. **14**, 1083 (2018).
- [24] M. Esterli, R. Otxoa, and M. Gonzalez-Zalba, *Small-signal equivalent circuit for double quantum dots at low-frequencies*, Appl. Phys. Lett. **114**, 253505 (2019).
- [25] R. Mizuta, R. Otxoa, A. Betz, and M. F. Gonzalez-Zalba, *Quantum and tunneling capacitance in charge and spin qubits*, Phys. Rev. B **95**, 045414 (2017).
- [26] S. Shevchenko, A. Omelyanchouk, and E. Il'ichev, *Multi-photon transitions in Josephson-junction qubits*, J. Low Temp. Phys. **38**, 283 (2012).
- [27] S. Shevchenko, S. Ashhab, and F. Nori, *Inverse Landau-Zener-Stückelberg problem for qubit-resonator systems*, Phys. Rev. B **85**, 094502 (2012).
- [28] G. Johansson, L. Tornberg, V. Shumeiko, and G. Wendin, *Readout methods and devices for Josephson-junction-based solid-state qubits*, J. Phys. Condens. Matter **18**, S901 (2006).
- [29] I. Ahmed, J. A. Haigh, S. Schaal, S. Barraud, Y. Zhu, C.-m. Lee, M. Amado, J. W. Robinson, A. Rossi, J. J. Morton, *et al.*, *Radio-frequency capacitive gate-based sensing*, Phys. Rev. Appl. **10**, 014018 (2018).
- [30] S. Chorley, J. Wabnig, Z. Penfold-Fitch, K. Petersson, J. Frake, C. Smith, and M. Buitelaar, *Measuring the complex admittance of a carbon nanotube double quantum dot*, Phys. Rev. Lett. **108**, 036802 (2012).
- [31] A. Betz, R. Wacquez, M. Vinet, X. Jehl, A. Saraiva, M. Sanquer, A. Ferguson, and M. Gonzalez-Zalba, *Dispersively detected Pauli spin-blockade in a silicon nanowire field-effect transistor*, Nano Lett. **15**, 4622 (2015).
- [32] M. F. Gonzalez-Zalba, S. N. Shevchenko, S. Barraud, J. R. Johansson, A. J. Ferguson, F. Nori, and A. C. Betz, *Gate-sensing coherent charge oscillations in a silicon field-effect transistor*, Nano Lett. **16**, 1614 (2016).
- [33] *See Supplemental Material at [URL will be inserted by publisher] for extra material on the quantum dot thermometer temperature sensitivity, electron thermometry error, quantum dot energy scales and coulomb peak location temperature dependence.*
- [34] W. H. Press, S. A. Teukolsky, W. T. Vetterling, and B. P. Flannery, *Numerical recipes 3rd edition: The art of scientific computing* (Cambridge university press, 2007).

Supplementary Material for ‘Non-galvanic calibration and operation of a quantum dot thermometer’

J. M. A. Chawner,^{*} S. Holt, E. A. Laird, Yu. A. Pashkin, and J. R. Prance

*Department of Physics, Lancaster University,
Lancaster, LA1 4YB, United Kingdom*

S. Barraud

CEA/LETI-MINATEC, CEA-Grenoble, 38000 Grenoble, France

M. F. Gonzalez-Zalba

*Hitachi Cambridge Laboratory, J. J. Thomson Ave.,
Cambridge, CB3 0HE, United Kingdom[†]*

(Dated: January 29, 2021)

arXiv:2012.01209v2 [cond-mat.mes-hall] 28 Jan 2021

^{*} j.chawner@lancaster.ac.uk

[†] Present address: Quantum Motion Technologies, Windsor House, Cornwall Road, Harrogate, England, HG1 2PW

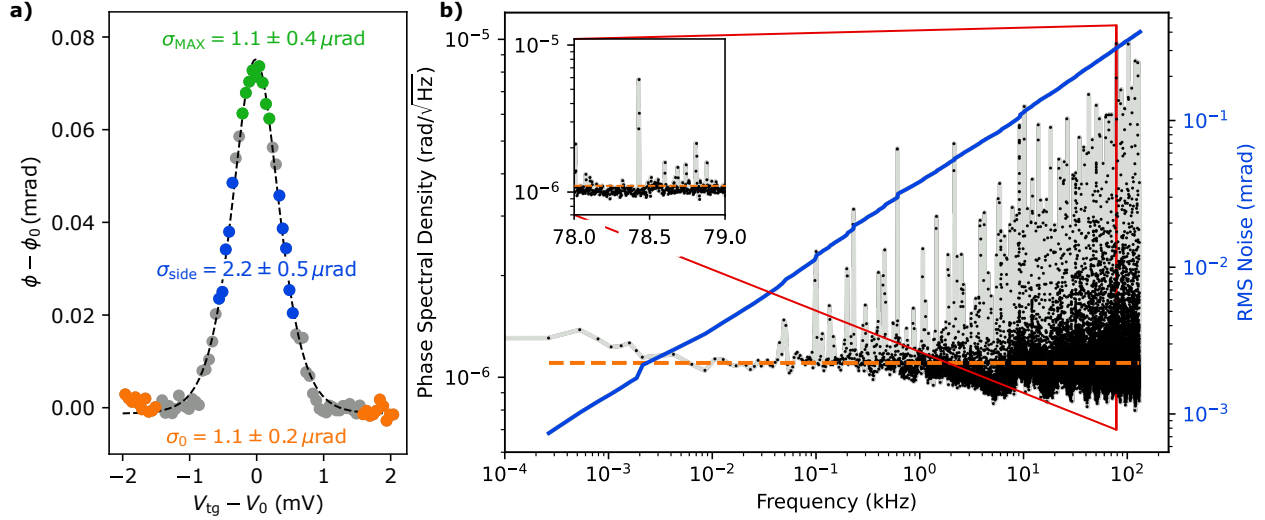


FIG. 1. Reflected phase modulation and noise measured in the dilution refrigerator. **a)** A phase trace taken at $T_f = 0.18\text{K}$. Each data point was measured for 3 seconds. The RMS phase noise for readings taken at the tails, σ_0 (orange), sides, σ_{side} (blue), and peak, σ_{MAX} (green), of the trace are equivalent, i.e $\sigma_0 \approx \sigma_{side} \approx \sigma_{MAX}$. The black dashed line shows a fit to the data that is used to estimate the RMS deviation of each point. **b)** An RF signal was reflected off the QD thermometer at $T_f = 8.7\text{mK}$, and a ADL5387 quadrature demodulator chip was used to extract the phase from the reflected signal. (This is detailed in the paper within the text and Figure 2a). The black points, connected with grey lines, show the spectral density of the readout. The orange dashed line corresponds to the average spectral density over the whole bandwidth, which is equal to a effective white noise phase sensitivity of $1.1 \pm 0.1 \mu\text{rad}/\sqrt{\text{Hz}}$. The inset displays a zoomed in section of the spectral density, which shows that the noise peaks seen at higher frequencies are extremely narrow compared to their typical spacing. The blue line shows the total RMS phase noise, which is the integral of the spectral density between 0.27 Hz and the frequency indicated.

I. DETERMINATION OF QD THERMOMETER SENSITIVITY

The sensitivity of the thermometer is determined by its response to temperature and the noise in the measurement of the phase of the reflected RF signal. Within the dilution refrigerator, a phase trace was measured at $T_f = 0.18\text{K}$, shown in FIG 1a). The RMS phase noise is consistent across the Coulomb peak, so it is assumed that the noise arises principally from the measurement chain and is not intrinsic to the device. It is presumed that any noise intrinsic to the QD, such as charge noise, lies somewhere underneath the measured noise floor. The reflected signal phase ϕ from the blockaded quantum dot (QD) was recorded at a sample rate of $2.6 \times 10^5 \text{s}^{-1}$ for 0.5 s. This

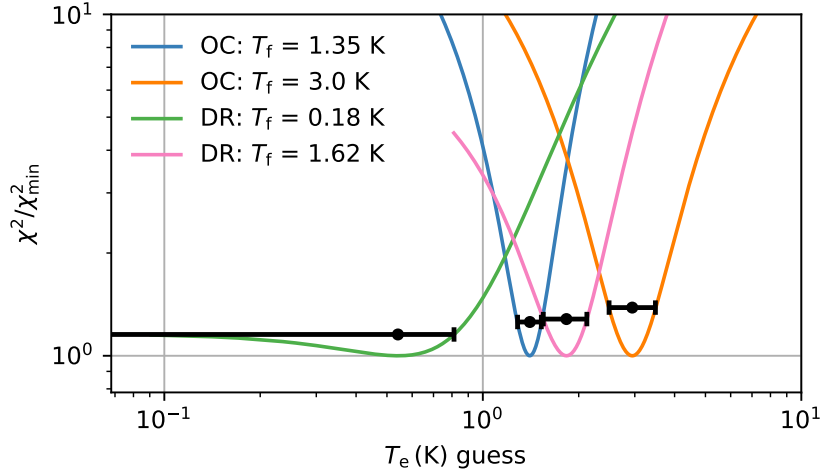


FIG. 2. Goodness of fit χ^2/χ_{\min}^2 against electron temperature T_e guess for a variety of phase traces. Two phase traces are from measurements taken within a cryogen-free, 1 K cryostat, ‘OC’, and were measured at $T_f = 3.0$ K and 1.35 K. Two more phase traces are from dilution refrigerator, ‘DR’, measurements taken at $T_f = 1.6$ K and 0.2 K. The black points represent the T_e fit where χ^2 is minimum. The height of these points is the confidence boundary $\chi^2 = \chi_{\min}^2 + 1$ which defines the confidence region shown by the error bars.

was done 128 times and averaged, producing the spectral density in FIG 1b). The result is generally flat, with narrow spikes of noise at higher frequencies. These spikes are much narrower than their typical spacing (most only having a single data point), therefore contribute relatively little to the total noise. In principle, they could be easily avoided with the use of a lock-in measurement technique. For example, a Zurich Instruments UHFLI could perform the demodulation and subsequently lock-in to a component of the demodulated signal. Averaging the spectral density over the entire bandwidth gives an effective white noise phase sensitivity of $1.1 \pm 0.1 \mu\text{rad}/\sqrt{\text{Hz}}$. Using $d\phi/dT_e$ from Eq. (7) in the paper text, with the condition $V_{\text{tg}} = V_0$, the phase spectrum can be converted to temperature spectrum. The best case phase reponsivity, $|d\phi/dT_e| = 0.10 \pm 0.01 \text{ mrad/K}$ at 3.0 K and $|d\phi/dT_e| = 0.24 \pm 0.02 \text{ mrad/K}$ at 1.3 K (from FIG 4 in the paper), gives a corresponding effective temperature sensitivity of $11 \pm 1 \text{ mK}/\sqrt{\text{Hz}}$ at 3.0 K, and $4.0 \pm 0.3 \text{ mK}/\sqrt{\text{Hz}}$ at 1.3 K.

II. ELECTRON THERMOMETRY UNCERTAINTY

The QD thermometer calibration process described in the paper text gives an estimation of α , Γ and A . These three constants are included in the phase model (described by Eq. (7) in the paper text), leaving only electron temperature T_e as a fitting parameter, along with ϕ_0 and V_0 which are trivial to define for each phase trace. For a given phase trace, each guess of T_e returns a goodness of fit that can be quantified with χ^2 via

$$\chi^2 = \sum_{i=0}^{N-1} \frac{[\phi^i - \phi(V_{\text{tg}}^i | T_e, \phi_0, V_0)]^2}{\sigma(N-3)}, \quad (1)$$

where N is the number of data points in the phase trace, ϕ^i and V_{tg}^i are the values of phase and top gate voltage respectively for the i^{th} data point [3]. The standard deviation of phase readout for each data point, σ , is constant over the whole phase trace. However, σ does vary for each trace, for example if the temperature is different. The minimum value of χ^2 , which we will label χ_{min}^2 , corresponds to the final fit estimate for T_e , and is always $\chi_{\text{min}}^2 < 10$. To work out the certainty of this measurement, a constant confidence boundary of $\chi_{\text{min}}^2 + 1$ surrounds χ_{min}^2 , creating an interval which represents one standard deviation of confidence. FIG 2 demonstrates this process with a few example phase traces; $T_f = 3.0\text{ K}$ and 1.35 K from the cryogen-free 1 K cryostat, $T_f = 1.6\text{ K}$ and 0.1 K from the dilution refrigerator. At temperatures below 1 K the confidence interval starts to broaden, and can extend to $T_e = 0$. At this point it can be said the QD thermometer has reached its lower temperature limit for operation. An explanation for the broadening of the confidence region is given in Section III.

III. ENERGY SCALES

Several energy scales are involved in the experiments that impact the behaviour of the QD. The tunnel coupling $\hbar\Gamma$ is measured from the QD thermometer calibration process. The QD excited state confinement energy E_{con} and QD charging energy $E_c = e\Delta V_{\text{sd}}$ can be observed in FIG 3 for both the 1K cryostat and dilution refrigerator experiments. To extract the voltage ΔV_{sd} , the average height was taken from the Coulomb diamonds on either side of the conduction resonance where the thermometry was performed. The thermal energy $k_B T$ is extracted from the range of temperatures used in each fridge during the experiments. All the energy scales for both systems are stated in Table I for comparison. For the cryogen-free 1K cryostat experiment, the QD energy

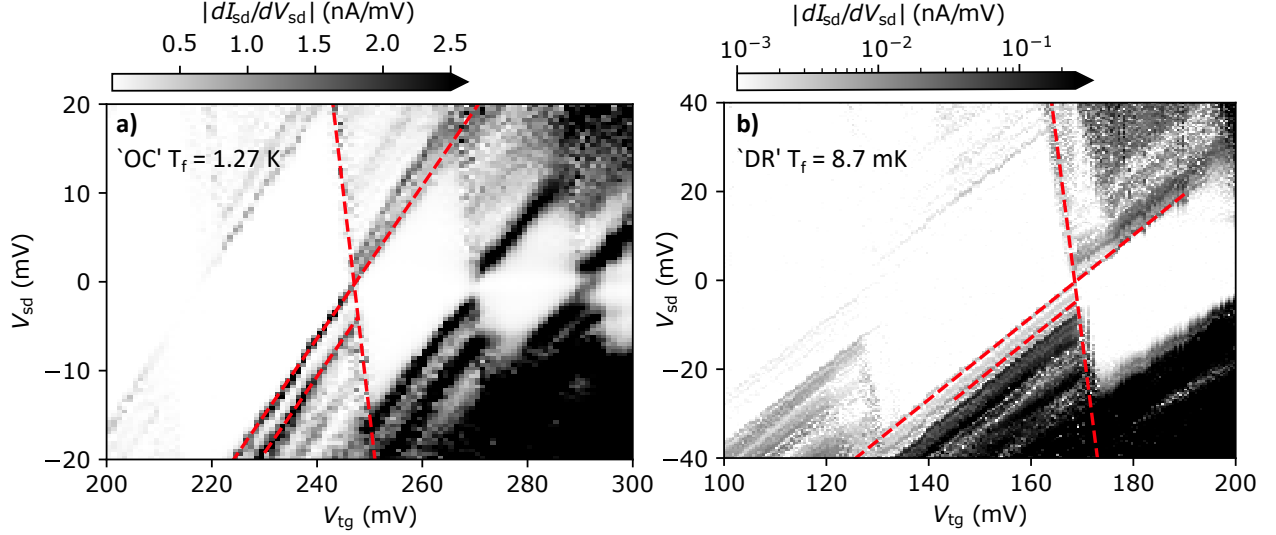


FIG. 3. Stability diagrams for QD in two fridge systems: **a)** a cryogen-free 1K cryostat ‘OC’ and **b)** a dilution refrigerator ‘DR’. V_{tg} is the top gate voltage, V_{sd} is source-drain voltage and I_{sd} is source-drain current. For each diagram, the crossed reds line highlight the Coulomb resonance where the thermometry was performed, and the gradients correspond to the lever arm as measured from the QD calibration process, $\alpha = 0.74 \pm 0.02$ and 0.84 ± 0.03 for OC and DR, respectively. The lowest red line highlights the first excited state of the QD.

| Energy Scale (meV) | $k_B T_e$ | $\hbar\Gamma$ | E_{con} | E_c |
|--------------------------|--------------|---------------|-----------|-------|
| Cryogen-free 1K cryostat | 0.12 – 0.26 | 0.18 | 3.7 | 16.9 |
| Dilution refrigerator | 0.015 – 0.14 | 0.32 | 4.2 | 28.8 |

TABLE I. Energy scales associated with the experiments in the two fridge systems. T_e is the electron temperature. The experiments took place over a range of temperatures, so the thermal energy scale is shown as a range. Γ is the QD tunnel rate which defines the tunnel coupling. E_{con} is the confinement energy for the first excited state in the QD. E_c is the charging energy for the QD.

condition is

$$k_B T_e \sim \hbar\Gamma < E_{con} < E_c, \quad (2)$$

so the Coulomb-blockaded QD is affected but not dominated by tunnel coupling. For the dilution refrigerator experiment the energy condition is

$$k_B T_e < \hbar\Gamma < E_{con} < E_c, \quad (3)$$

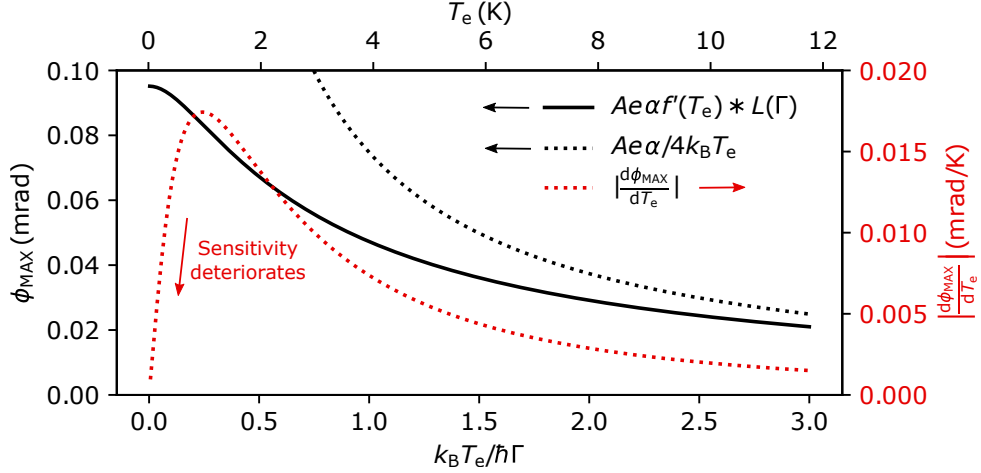


FIG. 4. Predicted maximum phase ϕ_{MAX} (solid black line) against electron temperature, when $V_{\text{tg}} = V_0$. The upper x-axis shows the electron temperature T_e and the lower x-axis shows the corresponding ratio between the thermal energy and tunnel coupling $k_B T_e / \hbar \Gamma$. The derivative of ϕ_{MAX} with respect to T_e is shown with a red dotted line. The prediction is generated from the thermometer calibration in the dilution refrigerator experiment detailed in section III of the paper text. The dotted black line shows the predicted ϕ_{MAX} assuming there is no tunnel coupling, i.e. $\Gamma = 0$, which will converge with the tunnel-coupled model at high temperature. Below $T_e = 1$ K the maximum phase ϕ_{MAX} begins to plateau, which indicates the loss of temperature sensitivity, and therefore the lower operational limit of the electron temperature.

so the Coulomb-blockaded QD is strongly tunnel-broadened and the tunnelling capacitance has much weaker temperature dependence.

In the case of the dilution refrigerator experiment, detailed in section III of the paper, the T_e readout uncertainty increases as the temperature is reduced below ~ 1 K. This occurs since the thermal energy scale is much smaller relative to the tunnel broadening, and so the phase trace shape has much weaker temperature dependence. This can be seen in FIG 4, which uses the predicted maximum phase of the phase trace, ϕ_{MAX} , as an indicator of the thermometer's temperature sensitivity. The prediction is based off the calibration of the QD thermometer in the dilution refrigerator experiment. At high temperatures, the tunnel coupling does not impact the thermometer phase significantly from the theoretical case of zero tunnel coupling. As the temperature is reduced to $k_B T_e / \hbar \Gamma \approx 2$, the maximum phase deviates significantly away from the prediction with negligible tunnel coupling. The sensitivity deteriorates at even lower temperatures where $k_B T_e / \hbar \Gamma \approx 1/4$, which in this particular case is $T_e \approx 1$ K. Approaching 0K, the phase

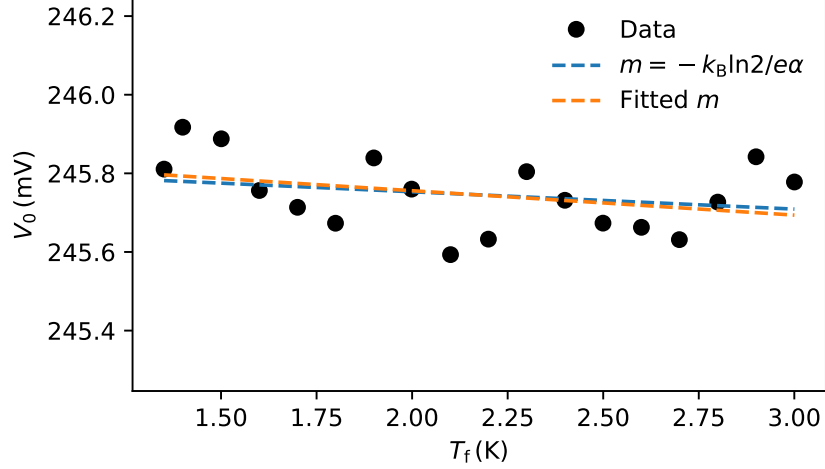


FIG. 5. Location of the top gate voltage V_0 where $P_{\text{QD}} = 1/2$, against fridge temperature T_f in the cryogen-free 1K cryostat. m equals the gradient dV_0/dT_f . The blue line shows the theoretical temperature dependence of V_0 with a gradient of $m = k_B \ln 2 / e \alpha \text{VK}^{-1}$. The orange line shows a linear fit to the data which predicts a gradient of $m = -(6 \pm 4) \times 10^{-5} \text{VK}^{-1}$.

trace converges on a Lorentzian shape defined by the tunnel broadening, and so the maximum phase plateaus, losing its temperature sensitivity. This defines the lower limit at which the QD thermometer can operate.

It has been shown that for a QD-reservoir system, the imbalance of spin degeneracy between an extra electron in the QD and the absence of an extra electron creates a temperature dependence for the QD energy with $1/2$ occupation probability, described by $E_{\text{QD}} = \mu \pm k_B T \ln 2$ [1, 2]. The top gate voltage value for $P_{\text{QD}} = 1/2$, labelled V_0 , is recorded for each phase trace measured across a range of temperatures. FIG 5 shows a subtle negative correlation between V_0 and the fridge temperature T_f . The theoretical gradient $dV_0/dT_f = -k_B \ln 2 / e \alpha \text{VK}^{-1} = -4.4 \times 10^{-5} \text{VK}^{-1}$ is certainly believable when compared with the measured V_0 , and a linear fit returns $dV_0/dT_f = -(6 \pm 4) \times 10^{-5} \text{VK}^{-1}$. Although the correlation is clouded by charge noise, the relationship between V_0 and T_f is consistent with the theory.

[1] I. Ahmed, A. Chatterjee, S. Barraud, J. J. Morton, J. A. Haigh, and M. F. Gonzalez-Zalba, *Primary thermometry of a single reservoir using cyclic electron tunneling to a quantum dot*, Commun. Phys. **1**, 1 (2018).

- [2] N. Hartman, C. Olsen, S. Lüscher, M. Samani, S. Fallahi, G. C. Gardner, M. Manfra, and J. Folk, *Direct entropy measurement in a mesoscopic quantum system*, Nat. Phys. **14**, 1083 (2018).
- [3] W. H. Press, S. A. Teukolsky, W. T. Vetterling, and B. P. Flannery, *Numerical recipes 3rd edition: The art of scientific computing* (Cambridge university press, 2007).